

INVESTIGATION OF VORTICAL STRUCTURES IN THE HUMAN PHARYNX/LARYNX REGION

A.-M. Shinneeb

Department of Mechanical and Materials Engineering
Queen's University
130 Stuart Street
Kingston, Ontario K7L 3N6
shinneeb@me.queensu.ca

Andrew Pollard

Department of Mechanical and Materials Engineering
Queen's University
130 Stuart Street
Kingston, Ontario K7L 3N6
pollard@me.queensu.ca

ABSTRACT

PIV measurements have been made at three locations in the pharynx/larynx region in the ETA model, one along the central sagittal plane and two cross-sectional planes. The measurements were made at a flow rate of 9.05 l/min which corresponds approximately to 10 l/min in the prototype. The corresponding Reynolds number Re based on the inlet condition is 673. Two thousand images were acquired at each location at a framing rate of 2 Hz. The mean velocity fields were then calculated. In addition, the data was analysed by the proper orthogonal decomposition (POD) technique to expose vortical structures. Only few modes were used for the POD reconstruction which recovered about 60% of the turbulent kinetic energy.

The results showed that the flow is characterised by regions of re-circulation, jet-like, and sink-like flows. In addition, the POD-reconstructed fields revealed the existence of energetic structures in the human pharynx/larynx region near the epiglottis. Some interesting features were observed in that region such as tearing and pairing processes, as well as the interaction between the flows induced by the structures.

INTRODUCTION

Aerosol drug delivery to the lungs using puffers is strongly dependent upon knowledge of the complex flow field generated in the human extra-thoracic airway (ETA) during the inhalation phase. That is, the human mouth provide significant geometrical obstacles to delivery of drug distal to the targeted location. Previous studies have found that 80-95% of an orally inhaled dose is deposited in the ETA and channelled to the gastrointestinal tract (see Johnstone et al., 2004). In order to maximize delivery to the targeted lung tissue, it is important to understand the human ETA flow field that could

drive the creation of alternate delivery mechanism to achieve minimal drug deposition in the ETA.

The complexity of the extra-thoracic airway (ETA) flow field also poses serious challenges for experimental measurement, and relatively few such measurements are available in the literature. Heenan et al. (2003) and Johnstone et al. (2004) studied experimentally the flow in an idealized human ETA using endoscopic particle image velocimetry (EPIV) and hot-wire anemometry (HWA) techniques, respectively. These experimental studies were planned to provide validation and confirmation for more detailed computer simulations. However, Ball et al. (2008), who studied computationally the flow field in the ETA using the lattice-Boltzmann method (LBM), demonstrated that EPIV and HWA measurements were not completely reliable when compared to results from a variety of turbulence models. Specifically, hot-wire measurements were not reliable in zones with recirculation and secondary flows, whereas EPIV measurements were influenced by optical access and seeding limitations. A complete discussion of the above problems is presented in the recent review by Kleinstreuer and Zhang (2010).

In an effort to understand the dependence of airflow on the geometry, Lin et al. (2007) investigated computationally the flow field in a realistic upper respiratory tract. The POD analysis of the flow revealed that the regions of high turbulence intensity were associated with a pair of counter-rotating vortex elements which extended from the laryngo-pharynx to the glottis. These structures resemble pulsating Taylor-Gortler-like vortices. They also found that the locations of these vortices coincide with the local maximum turbulent kinetic energy.

In this study, a transparent model with an index-matched working fluid was constructed and the particle image velocimetry (PIV) technique was used for the measurements.

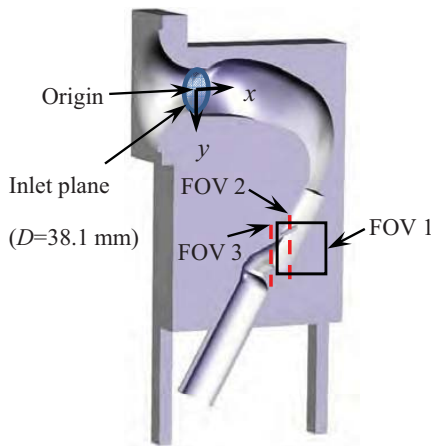


Figure 1. Geometry of the idealized ETA model which shows all basic anatomical features of the human ETA and the coordinate system. Note that the box and the dashed lines represent the position of the three fields-of-view (FOV) investigated in this study.

The main motivation behind this work is to provide insight into the structure of human ETA flow. This work is concerned with only the fluid mechanics of the inspired flow and does not attempt to consider the effect of these flow patterns on aerosol transport. Specifically, the objective of this study is to understand the flow field in the pharynx/larynx region in an idealized human ETA model. This was achieved by investigating the mean velocity and coherent structure fields which were exposed by the POD method.

MODEL GEOMETRY AND CONSTRUCTION

The geometry of the extra-thoracic airway (ETA) used in this study represents averaged-extra-thoracic airways geometry of healthy individuals is more practical. Figure 1 displays a sagittal view of this idealised ETA model. The idealised geometry possesses all the basic anatomical features of real ETA geometry. The main components of the ETA model include the oral cavity (mouth), the pharynx, the larynx, and part of the trachea. Note that the nasal cavity is not included in the model because it is assumed to be blocked off during oral inhalation. This design was developed based on information from magnetic resonance imaging (MRI) and computed tomography (CT) scans. The rationale behind the geometry and choice of dimensions are fully described in Stapleton et al. (2000).

The transparent flow passage needed for the PIV measurements was produced largely using the process described by Hopkins et al. (2000) which is summarized here. The flow passage was made by pouring a silicone-based material (Sylgard 184 silicone elastomer) around a rapid-prototype wax cast of the idealized ETA placed in a Plexiglas box. The wax cast was then flushed out with hot water, leaving an ETA replica within the clear silicone through which flows an index-matched aqueous glycerol. It was decided to use a double scale model to improve the accuracy of the measurements. This scale was also adopted by Heenan et al. (2003) and Johnstone et al. (2004) in their studies for similar reasons.

EXPERIMENTAL APPARATUS

The ETA model was installed in a closed re-circulating flow system. The experimental setup consists of a pulseless impeller pump, a feed reservoir, and a flow conditioner. The pump provided a steady flow and was regulated by a DC controller. After exiting the model, the working liquid (aqueous glycerol) returns to the feed reservoir. A bypass, contains a $1\ \mu\text{m}$ filter, was used to filter the working liquid before introducing the seed particles. The flow was conditioned at the inlet to the ETA model using a settling chamber and nozzle. After the flow conditioner, the cross-sectional flow diameter reduces at the entrance to the model by a circular arc exit (see Figure 1) with a radius equal to the inlet diameter (38.1 mm). The coordinate system used in this paper has its origin on the centre of the inlet nozzle with positive x to the right and y downward as shown in Figure 1.

The refractive index of the working fluid was matched with the model material by using a glycerol/water mixture in order to avoid optical distortion of the light scattered from the seed particles in the flow passage. The ratio of water to glycerol was approximately 39% to 61%, respectively. The refractive index was then measured using ATAGO PAL-RI refractometer and was 1.41. The experiments were carried out at a constant temperature of $26\ ^\circ\text{C}$. The dynamic viscosity and density of the mixture were measured and determined to be 8.49 cp and $1135\ \text{kg}/\text{m}^3$, respectively. Since the ETA model is scaled to a factor of 2 and the working fluid is different than air, the relationship between the model and the actual human ETA (the prototype) was established based on the Reynolds number Re . Thus, the flow rate reported in this paper is 9.05 l/min which approximately corresponds to 10 l/min in the actual human ETA.

PIV ANALYSIS

The PIV system used 120 mJ/pulse dual Nd:YAG lasers of 532 nm wavelength generated from a New Wave Research Solo PIV laser system. The light sheet was formed through a 250 mm focal length spherical lens and a $-25\ \text{mm}$ focal length cylindrical lens. The resulting light sheet was approximately 1 mm thick in the area of interest. After carefully filtering the water through a $1\ \mu\text{m}$ filter, silicon carbide seed particles were introduced. These particles have a specific gravity of 3.2 and a mean diameter of $2\ \mu\text{m}$ yielding a Stokes settling velocity of $0.00055\ \text{mm}/\text{s}$. Therefore, these particles are expected to faithfully follow the flow.

The field-of-view was imaged with a 2048×2048 pixel FlowSense camera operating in dual capture mode. Image analysis was performed with correlation analysis DynamicStudio v2.3 software developed by Dantec Dynamics. The images were analysed with 64×64 interrogation areas using the adaptive correlation between successive images. The interrogation areas were overlapped by 50%. The correlation peak was located within sub-pixel accuracy using a Gaussian curve-fitting method. This analysis process yielded a final interrogation area size of 32×32 pixels. Table 1 summarizes the size and resulting spatial resolution of the velocity fields reported in this paper. Note that the x - and y - locations in Table 1 represent the distance from the origin to the top left corner of the field-of-view. After the correlation analysis was complete, outliers were rejected using the cellular neural net-

Table 1. Summary of the characteristics of the velocity fields.

Field of view (FOV)	x -location (mm)	y -location (mm)	Image size (mm \times mm)	Spatial resolution (mm)
1	76.14	135.97	44.60 \times 44.60	0.35
2	94.27	133.81	48.76 \times 48.76	0.38
3	71.57	153.88	28.44 \times 28.44	0.22

work (CNN) method with the variable threshold technique of Shinnee et al. (2004). The percentage of vectors rejected was $\sim 4\%$. Rejected vectors were replaced using a Gaussian-weighted mean of their neighbours.

RESULTS

This section presents the PIV results in the pharynx/larynx region (see Figure 1). The flow rate is 9.05 l/min and the corresponding Reynolds number based on inlet conditions is 673. The mean flow and vortical structure results are presented below.

Mean Velocity Fields

The mean velocity was calculated from 2000 instantaneous velocity fields acquired at each location at a sampling rate of 2 Hz. Figure 2 shows a vector plot of the mean velocity field (FOV1) measured along the central sagittal plane ($z/D = 0$). The size and spatial resolution of the field-of-view is given in Table 1. Both x and y are normalised by the inlet nozzle diameter D . Note that the vertical distance y is positive downward. Also note that only every fifth velocity profile in the y -direction is displayed in the plot to avoid cluttering on the figure.

As shown in Figure 2, the cross-section of the flow at the top of the FOV is small because of the existence of the epiglottis (represented by a gray shape in Figure 2). Farther downstream, Figure 2 shows the formation of two recirculation regions; one behind the epiglottis (left side) and the other one in the bottom right side of FOV1 because of the proximity of the entrance to the larynx region (see Figure 1). It is obvious that the flow in this region is directed to the entrance of the larynx region and produces a laryngeal jet.

Figure 3 shows vector plots of the mean velocity fields measured in the y - z plane in the pharynx/larynx region at $x/D = 2.47$ and 1.88, respectively. Note that $z/D = 0$ represents the central sagittal plane of the model (see Figure 1). Figure 3(a) shows that the flow is mainly directed downward from the peripheries of the upper half of the flow field, and then form a recirculation zone in the lower central region of the FOV which is similar to the sink flow. Similarly, the vector plot shown in Figure 3(b), which represents the flow at downstream location, demonstrates similar behaviour. This indicates that the recirculation zones in both fields are correlated and extended downstream. Since the velocity component normal to the y - z plane is significant at these locations as can be seen in Figure 2, these plots indicate the three-dimensional nature of the flow.

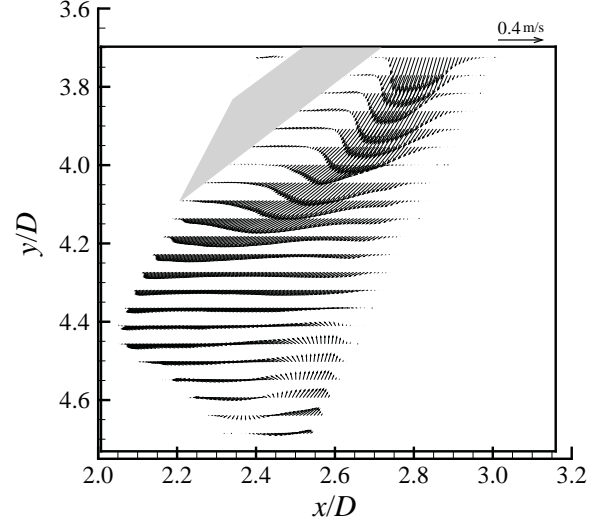


Figure 2. The mean velocity field obtained at the sagittal plane ($z/D = 0$) in the pharynx region (FOV1). The gray shape represents a cross-section of the epiglottis.

Coherent Structures

This section presents selected examples of large-vortical structures in the pharynx/larynx region educed by the proper orthogonal decomposition (POD) technique. The procedures may be summarized as follows. The POD method was applied by first averaging the velocity fields and calculating the fluctuating velocities. Then, the fluctuating velocity fields were processed using the POD via the method of snapshots (Sirovich, 1987). Two thousand velocity fields were used in this process, which yielded a temporal correlation matrix of size 2000×2000 . A complete description of the implementation of the POD using the method of snapshots may be found in Shinnee (2006). The number of modes used for the POD reconstruction in this paper was based on a target of $\sim 60\%$ energy content. These POD-reconstructed velocity fields provide an interesting set of flow visualization results obtained by a quantitative technique. The current results highlight the dynamics of large-energetic structures in this flow. It should be pointed out that the time separation between two consecutive velocity fields was 0.5 s which is large to follow the same vortical structures in successive frames. However, some interesting features can be captured from individual fields. It should be pointed out that this work produced a large amount of data, which cannot be presented here owing to space limitations. Consequently, only some selected examples are presented in this section.

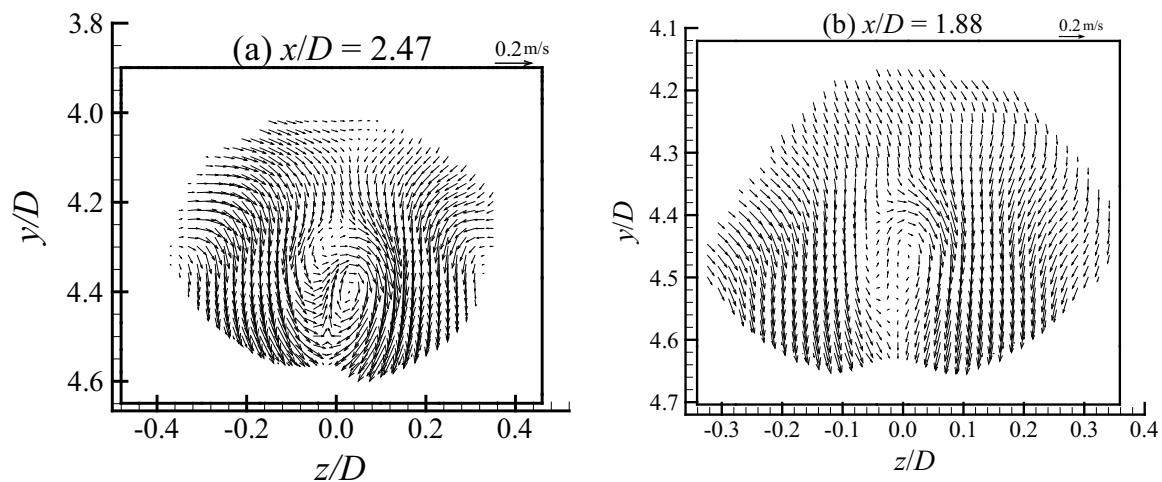


Figure 3. Mean velocity fields measured in the y - z plane at; (a) $x/D = 2.47$ (FOV2), and (b) $x/D = 1.88$ (FOV3). These velocity fields are obtained by averaging 2000 instantaneous velocity fields. Note that only every second vector is shown to avoid cluttering.

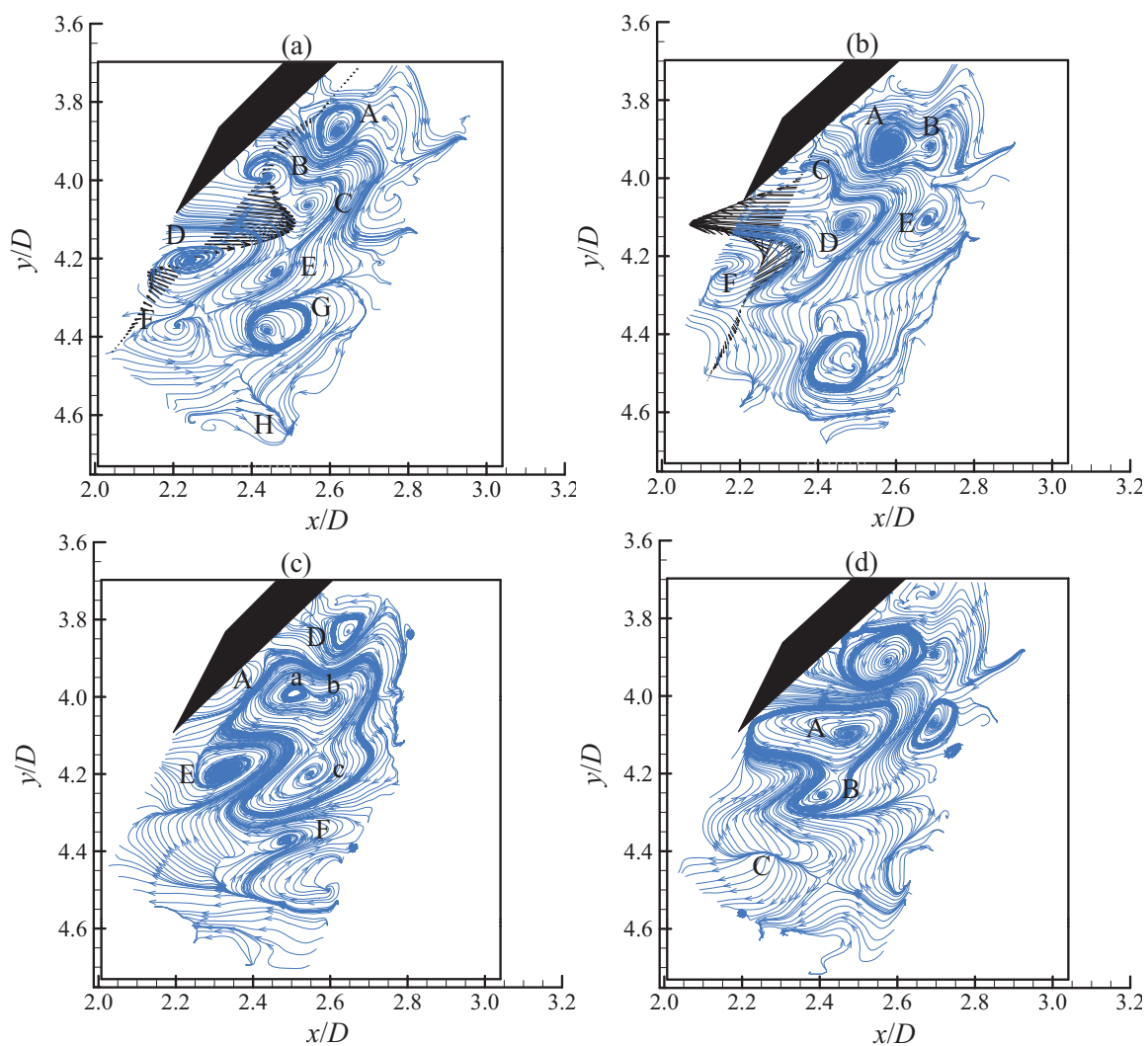


Figure 4. Four examples of POD-reconstructed fluctuation velocity fields (a), (b), (c), and (d) show vortical structures identified on the x - y plane along $z/D = 0$. The turbulent kinetic energy recovered in these fields is 62.1% using 3 modes.

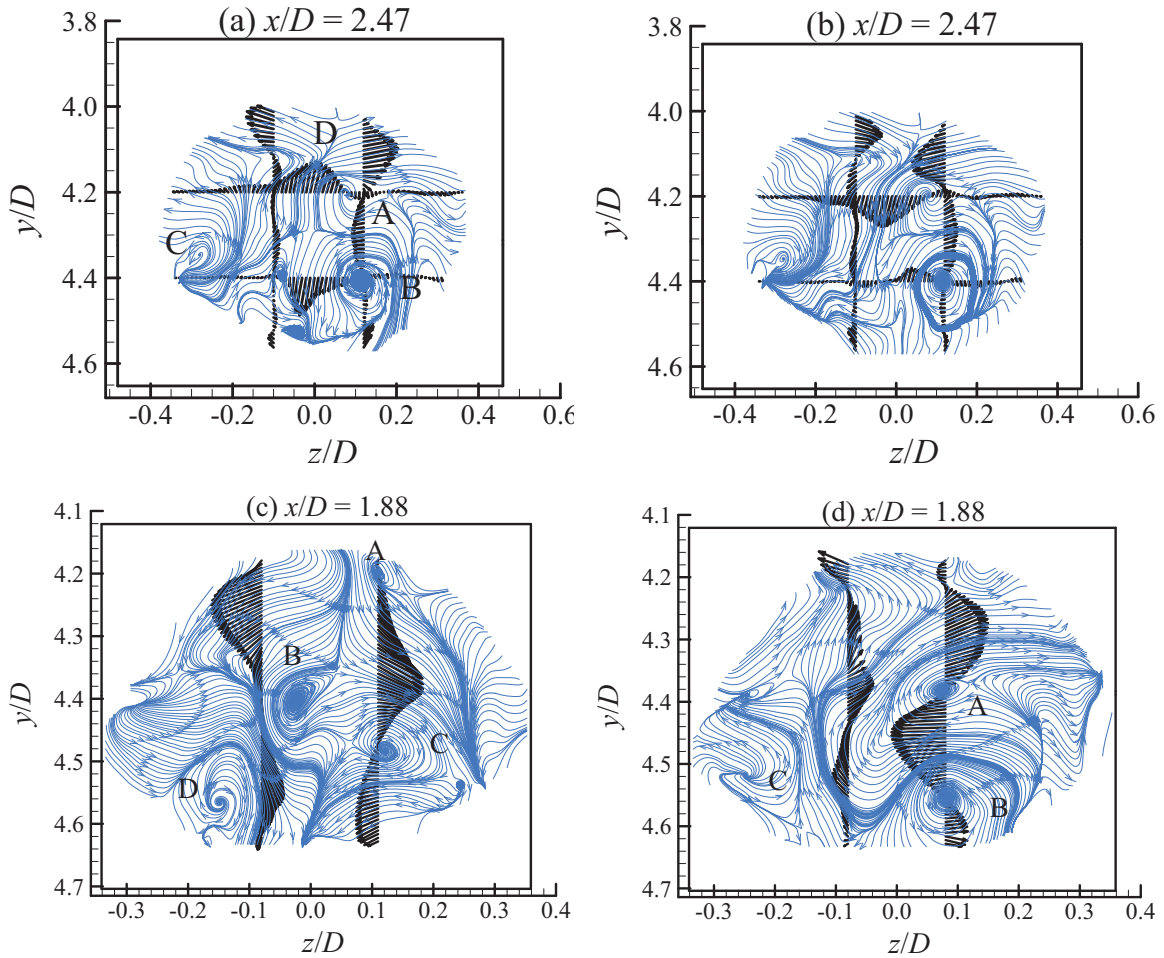


Figure 5. Streamline patterns of POD-reconstructed fluctuation velocity fields show vortical structures identified on the y - z plane; (a) & (b) along $x/D=2.47$, and (c) & (d) along $x/D=1.88$. The turbulent kinetic energy recovered in these fields is 61.4% using 6 and 2 modes, respectively. The induced flow by the structures is highlighted by superimposing velocity profiles at specific locations.

Figure 4 presents four selected examples of streamline plots to highlight the large-vortical structures in the central sagittal x - y plane ($z = 0$) of the ETA flow. The locations x and y are normalized by the inlet nozzle diameter D . Three modes were used for the reconstruction which recovered 62.1% of the turbulent kinetic energy. At first glance, all plots shown in Figure 4 illustrate that the flow contains a large number of counter-rotating vortical structures that are distributed throughout that region at all times. In addition, Figure 4 also illustrates the interaction between the induced flows by the structures.

Figure 4(a) shows several vortical structures that exist in pairs of opposite rotational sense. Specifically, the structures labelled A & B, B & D, D & E, E & G, and D & F are counter-rotating. However, some of these structures are unidirectional rotating vortices (e.g. structures labelled B & C, C & E, and E & F) which are close to each other. The unidirectional rotating structures (B, C, & E) seem to be originally one big structure before it is torn apart into three smaller cores. This figure also shows a jet induced by the two structures labelled B & D (see the superimposed velocity profile) which seems to be the reason of tearing the structures C & E, while structures B

& C could be torn apart by the effect of the induced flow of structure A. This induced jet is very similar to the mechanism of the ejection event that occurs near a solid wall. Another interesting feature is the inclined element that is labelled H where the direction of the flow at the sides of this thin element indicates that it is a side section of a vortical element.

Figure 4(b) also reveals several structures distributed throughout the flow field as pairs of clockwise (CW) and counter-clockwise (CCW) rotating vortices. The interesting feature is the jet, which is generated by three structures labelled C, D, and F, is directed toward the entrance to the larvnx (see Figure 1). An example of the occurrence of the tearing process in this flow may be shown by the presence of the two unidirectional rotating vortices labelled A & B. It appears that the formation of the two cores could be due to the induced flow by structures C, D, & E. Another example of the tearing process is shown clearly in Figure 4(c). This figure shows a large CW rotating structure (labelled A) with a large boundary and three cores labelled a, b, and c. This structure is surrounded by three CCW structures labelled D, E, and F. The strain fields produced by the vortices D & E could be responsible for splitting the structure core into three smaller cores

a, b, and c. The occurrence of the pairing process is also observed in this region which is illustrated in Figure 4(d) by the opposite rotational structures labelled A & B. The proximity and size of these structures as well as the limited space of the flow field appear to be the reasons of the occurrence of the merging process in this example. Figure 4(d) also shows an outward flow originating from the vortical element labelled C which is similar to the element labelled H in Figure 4(a).

To shed light on the vortical structures which are aligned normal to the y - z plane, Figure 5 shows four selected examples of POD-reconstructed velocity fields; (a) & (b) measured at $x/D = 2.47$, and (c) & (d) measured at a downstream location ($x/D=1.88$). The number of modes used for the reconstruction of fields (a) & (b) and (c) & (d) is 6 and 2, respectively, which recovered 61.4% of the turbulent kinetic energy. Figure 5(a) shows three structures whose axes are perpendicular to the y - z plane (labelled A, B, and C) and one vortex element whose axis is parallel to the y - z plane (labelled D). The flow induced by these structures is illustrated by superimposing four velocity profiles; at $z/D = 0.58$ and 0.80 , and at $y/D = 4.20$ and 4.40 . These profiles show that a jet flow is directed upward by structure A and then deflected outward to the right and left directions at the top of the flow field by the vortex element D. Similarly, a jet flow is directed downward by structure B which seems to flow upward again at the bottom edge. The velocity profiles shown in Figure 5(b) illustrate that the induced flow by the structures produced an inward horizontal jets near the top edge and also a vertical jet towards the centre of the FOV.

Similar to these structures can also be seen at the downstream y - z plane ($x/D = 1.88$) in Figures 5(c) and 5(d). Figure 5(c) shows that strong horizontal/downward jets (see the superimposed velocity profiles) are induced by the structures labelled A, B, C, and D whose axes are perpendicular to the y - z plane as well as to other structures that are not perpendicular to the plane (see the edges of the flow field). Figure 5(d) shows a large structure labelled A which is distorted by the structure labelled B. These structures (A, B, and C) appear to induce a strong horizontal/upward jet flow. Generally, the above results highlight the existence of strong vortical structures whose axes are normal to the x - y and y - z planes. These structures induce strong flow in all directions which indicate the three-dimensionality of the flow in this region. As well, some interesting features were observed such as pairing and tearing processes as well as bursting events (e.g. ejection-like event) near the epiglottis.

CONCLUSIONS

PIV measurements have been made at three locations in the pharynx/larynx region in the ETA model at a flow rate of 9.05 l/min which yielded a Reynolds number Re of 673. The following conclusions may be drawn from the analysis of the mean flow and POD results:

1. The flow is strongly three-dimensional and is characterised by re-circulation, jet-like, and sink-like mean flows;
2. The flow contains a large number of counter-rotating vortical structures that are distributed throughout the pharynx/larynx region at all times particularly whose axes are

normal to the x - y plane;

3. The region near the epiglottis in the pharynx is characterised by bursting events (e.g. ejection-like event); and
4. The interaction between the induced flows by the vortical structures appear to be responsible for the occurrence of tearing and pairing processes in that region.

Finally, the data presented in this paper shed light on the highly three-dimensional flow field; investigations continue to explore the complex flow nature in the human ETA.

REFERENCES

- Adrian, R. J., Christensen, K. T., and Liu, Z.-C., 2000, "Analysis and interpretation of instantaneous turbulent velocity fields", *Exp. Fluids*, Vol. 29, no. 3, pp. 275-290.
- Agrawal, A., and Prasad, A. K., 2002, "Properties of vortices in the self-similar turbulent jet", *Exp. Fluids*, 33(4), pp. 565-577.
- Ball, C. G., Uddin, M., and Pollard, A., 2008, "High resolution turbulence modelling of airflow in an idealised human extrathoracic airway", *Comput. Fluids*, 37, pp. 943964.
- Heenan, A. F., Matida, E., Pollard, A., and Finlay, W. H., 2003, "Experimental measurements and computational modeling of the flow field in an idealised human oropharynx", *Exp. Fluids*, 35, pp. 70-84.
- Hopkins, L. M., Kelly, J. T., Wexler, A. S., and Prasad, A. K., 2000, "Particle image velocimetry measurements in complex geometries", *Exp. Fluids*, 29, pp. 91-95.
- Hussain, A.K.M.F, 1986, "Coherent structures and turbulence", *J. Fluid Mech.*, 173, pp. 303-356.
- Jeong, J., and Hussain, F., 1995, "On the identification of a vortex", 285, pp. 69-94.
- Johnstone, A., Uddin, M., Pollard, A., Heenan, A., and Finlay, W. H., 2004, "The flow inside an idealised form of the human extrathoracic airway", 37, pp. 673-689.
- Kleinstreure, C., and Zhang, Z., 2010, "Airflow and particle transport in the human respiratory system", *Annu. Rev. Fluid Mech.*, 42, pp. 301-334.
- Lin, C.-L., Tawhai, M. H., McLennan, G., and Hoffman, E. A., 2007, "Characteristics of the turbulent laryngeal jet and its effect on airflow in the human intra-thoracic airways", *Respiratory physiology & Neurobiology*, 157, pp. 295-309.
- Robinson, S. K., 1991, "Coherent motions in the turbulent boundary layer", *Ann. Rev. Fluid Mech.*, 23, pp. 601-639.
- Shinneeb, A.-M., 2006, "Confinement effects in shallow water jets", Ph.D. thesis, Saskatoon, Saskatchewan: University of Saskatchewan.
- Shinneeb, A.-M., Bugg, J. D., and Balachandar, R., 2004, "Variable Threshold Outlier Identification in PIV Data", *Meas. Sci. Technol.*, 15, pp. 1722-1732.
- Sirovich, L., 1987, "Turbulence and the dynamics of coherent structures. Part I: Coherent structures", *Quarterly of Applied Math.*, 45(3), pp. 561-571.
- Stapleton, K. W., Guentsch, E., Hoskinson, M. K., and Finlay, W. H., 2000, "On the suitability of $k - \epsilon$ turbulence modeling for aerosol deposition in the mouth and throat: A comparison with experiment", *J. Aerosol Sci.*, 31(6), pp. 739-749.